Chapter 15
Terahertz Near-Field Imaging

Paul C. M. Planken, Aurèle J. L. Adam and DaiSik Kim

Abstract The terahertz (THz) frequency range has proven to be a very interesting frequency range for imaging applications. The smallest spatial features that can theoretically be resolved is limited by diffraction to values of about half of a wavelength, which corresponds to 150 μm for a frequency of 1 THz. To overcome this diffraction limit, THz near-field techniques have been developed. Some of these techniques are unique for the THz frequency range and others are derived from similar techniques used in, for example, the visible region of the electromagnetic spectrum. An interesting feature of many of these near-field techniques is that they measure the electric field rather than the intensity. This makes it also possible to study the near-electromagnetic field itself with a resolving power, as defined as the ratio of the spatial resolution to the wavelength, and bandwidth which are practically unobtainable in the visible region of the electromagnetic spectrum. This chapter describes a number of different techniques to overcome the diffraction limit in the THz frequency range and also the results that have been obtained with them.

P. C. M. Planken (✉) · A. J. L. Adam
Faculty of Applied Sciences, University of Technology Delft,
Lorentzweg 1, 2628 CJ Delft,
The Netherlands
e-mail: P.C.M.Planken@tudelft.nl

A. J. L. Adam
e-mail: A.J.L.Adam@tudelft.nl

D. Kim
Department of Physics and Astronomy,
Center for Subwavelength Optics,
Seoul National University, Seoul, Korea
e-mail: dsk@phya.snu.ac.kr

K.-E. Peiponen et al. (eds.), *Terahertz Spectroscopy and Imaging*,
Springer Series in Optical Sciences 171, DOI: 10.1007/978-3-642-29564-5_15,

15.1 Introduction: The Near-Field, the Far-Field, and the Diffraction Limit

15.1.1 The Diffraction Limit and the Far Field

In a conventional, far-field, imaging setup, the spatial resolution Δl is determined by the Rayleigh criterion as

$$\Delta l = 0.61 \frac{\lambda_0}{n \sin(\theta)}, \tag{15.1}$$

with λ_0 the wavelength of the light in vacuum, n the refractive index of the medium, θ half of the opening angle of the focused light beam, and $n \sin(\theta)$ the numerical aperture (NA) of the focusing element. For a typical terahertz (THz) imaging setup, with $f = 0.1\,\mathrm{m}$, $D = 0.05\,\mathrm{m}$, $\lambda = 300 \times 10^{-6}\,\mathrm{m}$, this gives $\Delta l \simeq 730\,\mu\mathrm{m}$. Tighter focusing will generally lead to smaller foci and thus an improved spatial resolution, but it is clear that the best obtainable spatial resolution in a THz far-field setup is totally inadequate for microscopy on a scale of $100\,\mu\mathrm{m}$ or less. A more graphic view of this is illustrated in Fig. 15.1. This figure shows calculations of the THz electric field around a perfectly conducting metal cylinder with a diameter significantly smaller than the wavelength and one with a diameter on the order of the wavelength. The field, which is incident from below, has a polarization which is perpendicular to the axis of the cylinder. For the large cylinder, a shadow effect is clearly visible even for distances of more than a wavelength behind and around the cylinder. This contrasts with the calculations for the small cylinder where the wavefront in the immediate vicinity of the cylinder is perturbed, but appears to have repaired itself at a distance from the cylinder larger than the cylinder diameter. Far away from the small cylinder, therefore, its presence, let alone its shape, can no longer easily be inferred from the light field.

15.1.2 The Near Field

Far-field imaging and spectroscopy on objects smaller than about half of a wavelength (NA $=$ 1) are therefore very difficult, especially at THz frequencies where light detection is not trivial. Figure 15.1 does show, however, that even a small object of sub-wavelength dimensions is clearly capable of affecting the light field, but only in a volume around the object comparable in size to that of the object itself. In this near-field then, the object is expected to be visible, provided we have a measurement method that allows us to exclusively measure the field in the immediate vicinity of the object. A good part of this chapter is therefore devoted to discussing the different ways in which this can be achieved in the THz frequency range.

The ability to perform imaging and spectroscopy on a sub-wavelength scale has a number of interesting applications in science and technology. These applications

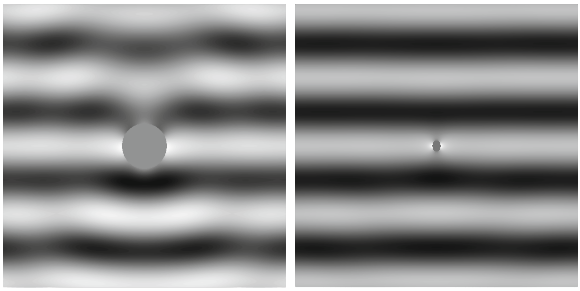

Fig. 15.1 A plane wave with a frequency of 0.2 THz is incident, from *below*, on two perfectly conducting metal cylinders: the *left figure* shows the calculated field distribution around a cylinder with a diameter of a 1,000 μm. The figure on the *right* shows the calculated field distribution around a cylinder with a diameter of 200 μm. *White* indicates positive electric field values, *black* negative. Note that for the small cylinder, the electric near-field immediately around the cylinder is significantly stronger than the incident field. This effect is much less pronounced for the larger cylinder

include the characterization of micro- and nanoscale devices, in particular the spatial distribution of the charge carriers, the characterization of small-volume molecular crystals, and measurements of the phase and magnitude of the electromagnetic field in the immediate neighborhood of subwavelength-sized metal structures such as holes in metal films and metamaterials. Charge carriers can be observed with great contrast because spatially varying carrier densities in real nanoscale transistors, correspond to spatially varying plasma frequencies in the THz range, ensuring a large contrast. Organic and inorganic crystals can be observed because they have unique phonon absorption spectra or phonon-like absorption spectra in the THz frequency range, each THz spectrum constituting a spectral fingerprint of the material. These spectral fingerprints even allow the identification of polymorphs of the same molecule. The electromagnetic field around tiny metal structures, finally, can be studied in extraordinary detail because of the unique property of the technique used for this, THz time-domain spectroscopy, that it measures the *electric field*, rather than the intensity of the light.

15.2 Apertureless Near-Field Microscopy

Apertureless near-field scanning optical microscopy (ANSOM) is based on the idea that the sub-wavelength-sized apex of a tapered metal tip can scatter light and thus act as a tiny source. Bringing the tip close to an object changes the dielectric environment of the tip and thus the amount of light scattered from it, as schematically illustrated in Fig. 15.2a. By measuring the amount of scattered light as the tip is scanned across the object, information on the position-dependent dielectric properties of the object can be obtained with a sub-wavelength spatial resolution. Pioneering experiments

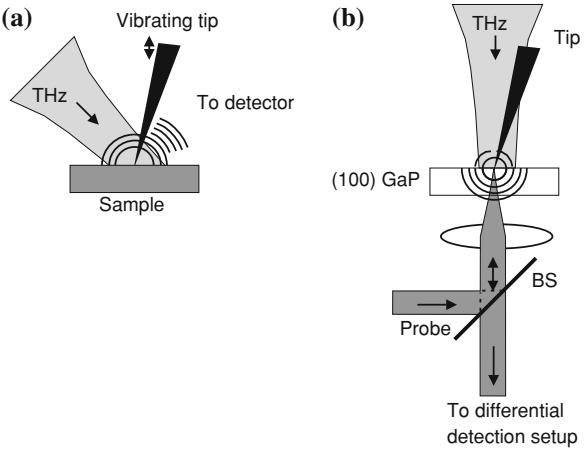

Fig. 15.2 Illustration of THz ANSOM. **a** A THz field incident from above illuminates the tip which is held above a sample/substrate. Light scattered by the tip is collected in the far-field; **b** a metal tip, held above a sample/substrate is illuminated with a THz beam, in this case a single cycle pulse. The tip apex concentrates the electric field to a small sub-wavelength sized region underneath the tip and is detected in the near-field in a GaP electro-optic crystal, using a tightly focused, near-IR probing pulse

using metal tips were performed at visible and infrared wavelengths [1–5]. The first THz ANSOM experiments were performed using THz pulses in a time-domain spectroscopy setup [6, 7]. The near-field of the tip could be measured directly by electro-optic sampling of the field near the tip apex using a focused probe pulse, as illustrated in Fig. 15.2b. An interesting aspect of this approach is the ability to suppress unwanted background signals by a proper choice of the electro-optic crystal orientation. It can be shown that a (100) oriented GaP or ZnTe crystal is capable of measuring the z-component of the electric field, corresponding to the field component perpendicular to the crystal surface, while being blind to the x and y components [6, 8]. A z-component is present only near the tip apex, something which, in the quasi-static approximation, can easily be understood from the boundary conditions of the electric field at a metal surface which only allow the existence of a field component perpendicular to the metal. Note that this is true for a perfect metal only, as for a real metal a small but non-zero tangential component is allowed. This component is very small at THz frequencies and will be ignored for the remainder of this chapter. Near the tip apex therefore, the field lines are distorted and a z-component is created. A spatial resolution of about 5 μm was obtained in this way, limited by the probing beam focal diameter. These experiments differ from visible/infrared ANSOM experiments in that they are capable of measuring the near electric-*field* rather than the intensity, which, as we will show below, allows one to measure frequency filtering properties of these metal tips. A somewhat different approach, in which a tapered metal tip was used as a probing antenna, predominantly sensitive to the z-component of the near-field, was also shown to be capable of reaching a sub-wavelength spatial resolution [9].

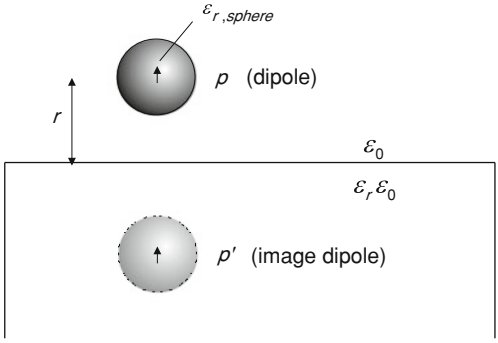

Fig. 15.3 Illustration of a sphere, illuminated with THz light, held above a dielectric half-plane. In the sphere model, the sphere is polarized and subsequently replaced by a point dipole of the corresponding strength. The formation of an image dipole is also taken into account. Note that compared to a perfect metal, the image dipole for a dielectric half-plane is weaker

In another THz ANSOM technique, the field scattered by the tip is measured in the far-field in the specularly reflected direction [10–12]. This means that the signal is superimposed on a large background but, nonetheless, a 150 nm spatial resolution was claimed in these experiments.

In yet another beautiful experiment in which the light source was a THz continuous gas laser, a parabolic mirror was used to measure the backscattered light from a metal tip, and a spatial resolution down to 40 nm was reported [13]. In many ANSOM experiments, the tip is vibrated in a direction perpendicular to the sample surface. When combined with lock-in detection at the vibration frequency, or at a higher harmonic of the vibration frequency, the background signal coming from light scattered off the tip shaft is strongly reduced and the spatial resolution is strongly improved. The reason for this improvement becomes clear when the scattered signal is measured as the tip approaches the sample surface. Such a measured approach curve shows that the near-field signal depends in a highly nonlinear fashion on the tip/sample distance, dramatically increasing just before the tip touches the sample. When we think of the tip as a series of oscillating dipoles, each having an electric near-field that decays with the cube of the distance, it is the dipoles closed to the apex which give the strongest nonlinear variation in the near-electric field versus tip/sample distance [14]. This nonlinear behavior translates into higher harmonics of the modulation signal and by detecting the signal at these harmonics, the signal contribution from regions of the tip other than the apex, are strongly suppressed. Only light scattered near the apex is strongly modulated by the oscillating tip/sample distance and thus more effectively measured than light scattered off the shaft. In ANSOM experiments, the amount of light scattered by the tip increases dramatically when the tip approaches the surface. In a simple, quasi-static, model which treats the tip as a small sphere, Knoll and Keilmann show that this is in part due to the near-field interaction between the tip and the surface [4]. Suppose that we have an incident field (-component) perpendicular to the surface. This field polarizes the sphere, thus creating a dipole moment $p = 4\pi\varepsilon_0 R^3 E_0 \frac{\varepsilon_{r,\text{sphere}}-1}{\varepsilon_{r,\text{sphere}}+2} \equiv \alpha E_0$, with E_0 the amplitude of the incident field, R the radius of the sphere, $\varepsilon_{r,\text{sphere}}$ the relative permittivity of the sphere material, and α the polarizability of the sphere (Fig. 15.3). This dipole, in

turn, induces an image dipole in the materials underneath. The *total* dipole moment of the system then becomes [4]:

$$p_{\text{tot}} = \frac{\alpha(1+\beta)}{1-\dfrac{\alpha\beta}{16\pi r^3}} E_0 = \alpha_{\text{eff}}^{\perp} E_0, \tag{15.2}$$

with r the distance of the dipole to the surface, $\beta = \frac{\varepsilon_r - 1}{\varepsilon_r + 1}$, ε_r being the relative permittivity of the sample, and $\alpha_{\text{eff}}^{\perp}$ the effective polarizability of the whole sphere/sample system. The scattering cross-section being proportional to $|\alpha_{\text{eff}}^{\perp}|^2$, the equation shows that when the surface is approached and r thus becomes smaller, the amount of scattered light increases rapidly. The model is very simple, but provides excellent physical insight into the scattering process, even though it contains considerably approximations, such as the assumption that the field created by the image dipole at the position of the original dipole is homogenous. However, something that is not explained by the sphere model is the measured characteristic frequency response of the metal tips used in THz ANSOM experiments. It was shown that metal tips can behave rather more like low-pass filters, reducing the bandwidth available in the near-field in THz ANSOM experiments [15–19]. This can be understood from the fact that the metal tip acts more like a wire antenna than like a sphere. The sphere model also tends to underestimate the absolute value of the field strength underneath the metal tip compared to the antenna model as antennas are capable of collecting more light. In the quasi-static approximation, and assuming that the wire is much shorter than the wavelength, the wire antennas can be treated as a series of dipoles having a position-dependent strength (Fig. 15.4a) [14, 20]. This strength follows a triangular distribution as a function of position along the wire, mimicking the triangular current distribution assumed in the wire, as shown in Fig. 15.4b. The antenna has a length d and is held vertically at a distance a above a dielectric half-plane having relative permittivity ε_r. It can be shown that the z-component of the electric field at a position (x, y, z) underneath the antenna, inside the dielectric can be written as [14, 20]:

$$E_z \propto \frac{1}{4\pi\varepsilon_0(1+\varepsilon_r)} \left(\frac{1}{R_a} + \frac{1}{R_b} - \frac{2}{R} \right), \tag{15.3}$$

with $R^2 = x^2+y^2+(z-\frac{a+b}{2})^2$, $R_a^2 = x^2+y^2+(z-a)^2$, and $R_b^2 = x^2+y^2+(z-b)^2$. Note that R_a, R_b, and R, represent the distance from the point (x, y, z) to the bottom, the top, and the midpoint of the antenna, respectively. Physical insight can be obtained when we look at the field at position $(0, 0, 0)$, underneath the antenna, just inside the dielectric. If we further assume that $a \ll b$, corresponding to a tip/sample distance which is small compared to the tip length, we can approximate the expression by

$$E_z \propto \frac{1}{4\pi\varepsilon_0(1+\varepsilon_r)} \frac{1}{a}. \tag{15.4}$$

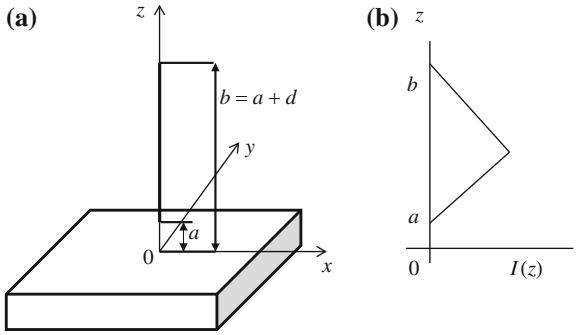

Fig. 15.4 **a**. Principle of THz aperture-less microscopy. A metal tip of length d, held at a distance a from a surface, is illuminated with a THz beam, in this case a single cycle pulse. The tip apex concentrates the electric field to a small sub-wavelength sized region underneath the tip. Light scattered by the tip/sample combination is collected in the far-field. Often, the tip is vibrated to suppress contributions to the signal by light scattered off the tip shaft . **b** Triangular current distributrion assumed to be present in the tip

This should be compared to the field of a vertically oriented point dipole, not taking image-dipole effects into account, which falls off as $1/a^3$. The physical/mathematical reason for the $1/a$ decay is not only that in the description of the antenna, we have many dipoles instead of just one but, also, that on the antenna, the strength of these dipoles increases linearly with distance to the apex, as it should for a short linear wire antenna. As the metal is retracted from the surface, therefore, the field of the wire antenna falls off much more slowly than the field of a point dipole, something that has been observed experimentally as shown in Fig. 15.5, where we plot the measured electro-optic signal as a function of tip-substrate distance [14]. Note that the signal plotted in this figure does *not* correspond directly to the actual THz electric field. Rather, it represents the integral of the electric field taken over a distance in the electro-optic crystal of 150 μm.

This slow decay is caused by the contribution to the field by the tip shaft, which obviously cannot be ignored. Interestingly, the $1/a$ dependence predicted by the antenna model agrees with the model by van Bladel [21] and Cory et al. [22]. They treat the tip apex as a small cone, and when the cone angle approaches zero, as should be the case for an infinitely thin wire antenna, they obtain the same $1/a$ dependence. The wire antenna model, however, has its shortcomings too. In the above form, it ignores image dipole effects and it assumes that the wire is infinitely thin. It should therefore be considered complementary to the sphere model only. As the tip is vibrated, the source of the field detected synchronously with the vibration, will mostly be located close to the tip apex, since the fields of the dipoles located closest to the apex and thus closest to the surface of the dielectric will be modulated the most. We stress, however, that the frequency contents and the strength of the measured signal are determined by the response of the *entire* antenna to the incident field, not just the apex. One aspect of apertureless near-field microscopy has not been

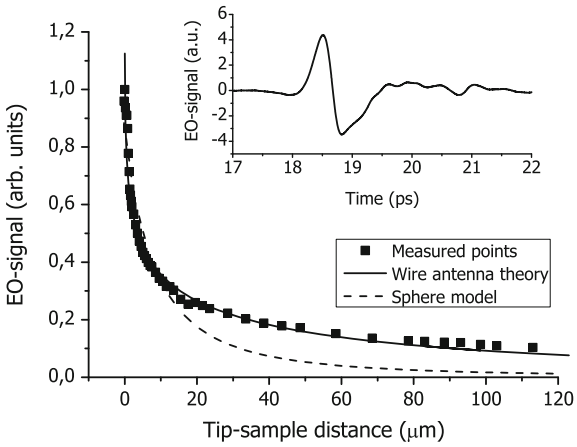

Fig. 15.5 Electro-optic signal measured underneath a tapered copper wire used in a THz ANSOM experiment, as a function of the tip-substrate distance. The substrate is a (100) oriented GaP electro-optic crystal. The *solid curve* represents the electro-optic signal based on the antenna model, the *dashed curve* the electro-optic signal based on the sphere model. Clearly the sphere model fails to reproduce the relatively slow decay observed for larger distances. The *inset* shows the electric near-field measured when the tip-substrate distance is 1 μm. The crystal thickness is 150 μm. Adapted from [14]

mentioned so far. The amplitude of the signal from the tip-sample system is as much determined by the dielectric function of the sample as by the distance between the tip and the sample. This means that care must be taken to avoid confusing variations in tip-sample distance with variations in the dielectric properties of the sample. This can be done, for example, by measuring on topographically flat samples or by measuring the response as a function of THz frequency so that absorption resonances in the sample can clearly be identified.

15.2.1 Variations on the ANSOM Theme

Rather than directly illuminating the tip near the apex, it is also possible to use the guiding properties of the tip to transport the THz radiation to the apex. The radially polarized waves on these wires, also called Sommerfeld waves, can propagate relatively long distances, on the order of several tens of cm's and show a very high potential for applications in THz imaging and micro-spectroscopy. The first clear demonstration of the creation and propagation of these waves at THz frequencies was given by Wang and Mittleman [23]. In subsequent publications various aspects, related to the dispersion, propagation, and confinement near the apex of the wire, were reported [24–27]. A coaxial geometry, made of a wire centered inside a hole in a metal plate surrounded by surface corrugations, was also studied as a way to

excite the Sommerfeld wave [28]. Another method to excite this mode is by exciting the wire with a radially polarized wave created by excitation of a radially symmetric photoconductive emitter [26, 29]. In addition, it was shown how these Sommerfeld waves on tapered wires can be used to do near-field imaging [30, 31]. We note that numerical simulations suggests that propagation of THz light toward the end of a corrugated, tapered metal wire should give rise to strongly localized fields near the apex [32, 33]. This may also give rise to strong THz fields near the tip apex which holds promise for THz nonlinear optics on the micro- and nano-scale, using moderately strong THz sources.

15.3 Aperture Techniques

One way to increase the spatial resolution in THz imaging is to use small, sub-wavelength sized, apertures to reduce either the size of the source, the size of the detector, or both. One of the earliest experiments in this direction at THz frequencies was first performed by Keilmann [34] and later by Hunsche et al. [35] who both used conical tapered, metal waveguides with a small exit aperture to reduce the size of the THz source. A spatial resolution on the order of $\lambda/2$ was obtained by Keilmann and $\lambda/4$ by Hunsche et al. One of the problems of using apertures is that the far-field power transmission of a small aperture scales as a^6, with a the diameter of the aperture [36–38]. For wavelengths $<\lambda/2$, therefore, the far-field transmission decreases very rapidly indeed. A somewhat different approach was taken by Mitrofanov et al., who decreased the size of THz source by integrating a small aperture in a metallic layer with a photoconductive emitter, to obtain a small source giving a spatial resolution of about 60 μm [39]. In subsequent papers Mitrofanov et al. [40] also explored the possibility of integrating small apertures with photoconducting antennas, for the *detection* of THz pulses. With this collection mode detector, of which an example is shown in Fig. 15.6, an impressive spatial resolution of 7 μm was eventually obtained [41]. For an electric field measurement, the far-field transmission scales with the aperture size as a^3. This was confirmed in a THz experiment using apertures as small as 5 μm, integrated on a photoconducting detector [41]. For apertures this small, the tiny but measurable direct transmission through the 600 nm thick metal layer, in which the aperture is defined, can no longer be neglected. In a separate experiment, the same authors increased the distance between the detector and the hole and found that the field decays inversely proportional to this distance [42, 43].

The property of THz time-domain spectroscopy, namely that it is capable of measuring the electric field rather than the intensity, is clearly an advantage when measuring the transmission properties of small holes in the near-field. It was found, for example, that the near-field measured directly behind an aperture can be viewed as the time-differentiated version of the incident field. This was first observed by Mitrofanov et al. [44, 45] using an aperture in close proximity to a photoconductive antenna, as shown in Fig. 15.7, and later by Adam et al. [46] using near-field electro-optic sampling behind an aperture integrated on an electro-optic detection crystal.

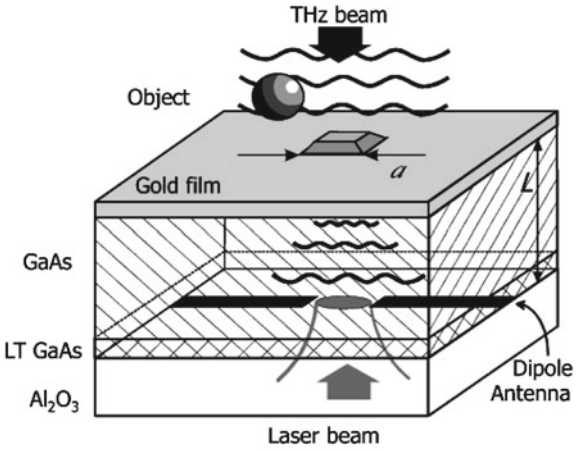

Fig. 15.6 Schematic diagram of the near-field probe used by Mitrofanov et al. [40]. A photoconductive dipole antenna is fabricated on LT GaAs and transferred to a sapphire substrate. The GaAs substrated is thinned and a GaAs cone is formed on top. A 600 nm gold film is deposited on the surface, except in the area of the cone, forming the aperture. Adapted from [41]

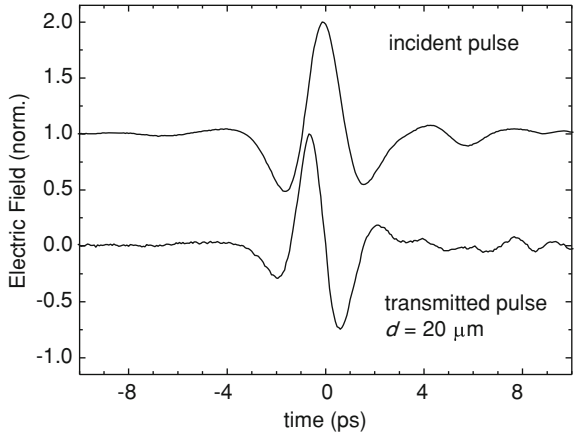

Fig. 15.7 Measured incident THz electric field and THz electric field transmitted by a 20 μm diameter aperture in a gold film, using the device shown in Fig. 15.6. The electric field transmitted by the aperture is clearly the time-derivative of the incident electric field. Adapted from [45]

This differentiation should, perhaps, not come as a surprise as this was also predicted by Bouwkamp, who calculated the near-field behind a circular hole in an infinitely thin, perfectly conducting screen, further assuming that the aperture diameter was much smaller than the wavelength. For example, the expression found by Bouwkamp [37, 38] for the electric near-field component perpendicular to the metal surface, E_z, is:

$$E_z = E_0 \frac{4i}{3} ka \frac{a/\rho}{\sqrt{\rho^2/a^2 - 1}} \cos(\phi), \quad \rho > a \tag{15.5}$$

with a the radius of the hole, ρ the radial coordinate, ϕ the azimuthal angle, E_0 the incident electric field amplitude and k the wavevector of the incident radiation. Note that this equation is valid only in the plane of the metal at $z = 0$, where for $\rho > a$ only E_z is nonzero, as dictated by the boundary condition for the component of the

electric field perpendicular to a perfect metal. Inside the hole at $z = 0$, E_z is zero too. For the in-plane components of the field the reverse is true: at $z = 0$ there can only be a field in the aperture, as the boundary condition for the parallel component dictates that it should be zero at the surface of a perfect metal.

The multiplication of the incident field with the term $ik \propto i\omega$ in the frequency domain, corresponds to differentiation of the THz field in the time-domain [46]. This is reminiscent of the properties of a high-pass filter in electronics and again a reminder that metal structures in general have a frequency-dependent response with associated phase shifts in the transmitted electric field. Other aspects of the model by Bouwkamp have been tested as well, such as the 2D distribution of the field around apertures. Measurements of this will be treated in more detail in the next section. Clearly, the model has its limitations too. For example, Eq. 15.5, predicts infinitely strong electric fields at the edge of the aperture which is physically impossible. However, as we will show in more detail later, the model is capable of explaining many features of THz near-field measurements performed on apertures. For a fixed value of ρ/a for example, Eq. 15.5 shows that the near-field component E_z decreases *linearly* with aperture size a, in sharp contrast with the a^3 dependence for the far-field. For a still small, nonzero, distance to the hole, the dependence of the transmission is neither linear nor cubic. This agrees well with measurements of E_z close to the edge of a circular aperture for three different aperture diameters [46]. To enhance the total transmission through an aperture, the aperture can be surrounded by a bull's eye structure [47–50]. This structure consists of concentric grooves or a grating structure around a small aperture. When the grooves are illuminated, surface waves are created in which funnel additional energy through the aperture, thereby enhancing the total transmission. As the structure is periodic, the enhancement, however, comes at the cost of a narrower bandwidth.

Apertures, of course, do not have to be circular. By using a bow-tie shaped hole in metal film, surrounded by a bull's eye structure, Ishihara et al. managed to obtain a significant, enhanced transmission and a subsequent spatial resolution of $\lambda/17$ [51, 52].

15.3.1 Waveguides, Dynamic Apertures and Quasi Apertures

Parallel plate waveguides [53], may also be used for THz microscopy [54]. By adiabatically tapering the width and the separation of two parallel plates, Zhan et al. [55] were able to confine THz light to an area of $10 \times 18\,\mu\text{m}^2$. In the latter example, near the edges of the waveguide the light is not physically confined by the metal as in a regular metal waveguide which is fully closed in all directions perpendicular to the propagation direction, but confinement occurs nonetheless.

It is not always necessary to use a real physical aperture in a metal film to perform aperture microscopy. Chen et al. [56, 57] used an intensity-modulated, focused, optical gating beam on a semiconductor wafer to modulate a very small portion of a THz beam. In a sense, the gating beam induces an inverse aperture, or metallic disc,

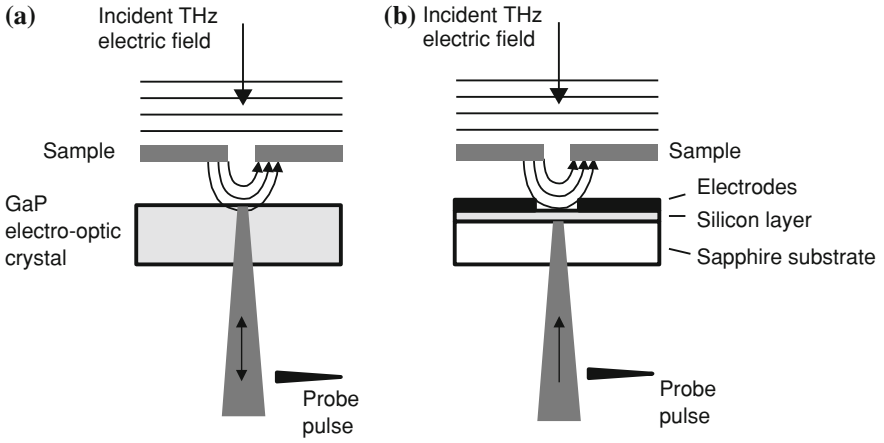

Fig. 15.8 Two different near-field detection methods. **a** A sample, illuminated with a THz pulse, is held close to an electro-optic crystal. The THz electric near-field is sampled with a sub-wavelength spatial resolution using a focused probe pulse; **b** a sample is held in the near-field zone of a small photoconductive antenna detector, gated by a probe pulse. The small dimensions of the antenna structure guarantee a sub-wavelength spatial resolution

to distort a sub-wavelength sized part of the beam. By holding a sample close to the wafer and by detecting only the modulated part of the THz beam, this "dynamic aperture" technique allowed for a 50 μm spatial resolution.

When electro-optic detection is used to measure the THz electric field, a tightly focused probing beam can be used to detect the THz electric near-field in a small volume, as shown in Fig. 15.8a. This method circumvents the THz diffraction limit because the near-IR probing beam has a much smaller wavelength than the THz beam and can thus be focused to much smaller spot sizes [6, 46, 58]. Loosely speaking, the probing beam acts like a detection aperture which limits the sampling area to very small values. It is reminiscent of the electro-optic sampling technique based on the use of specially shaped $LiTaO_3$ crystal to probe local THz electric fields on striplines and resonators [59, 60].

The advantage of using this technique is that it allows for the separate detection of all three vector components of the electric field by proper choice of the electro-optic crystal orientation. With a (100) crystal orientation, for example, the component of the electric field perpendicular to the (100) surface, E_z can be measured [6, 8]. Using a (111) crystal orientation, the components of the electric field parallel to the (111) crystal, E_x and E_y, can be measured separately as well [61]. In principle, a (110) crystal orientation can be used too to measure the in-plane components, but the advantage of using a (111) crystal is that only a rotation of the probe beam polarization vector over 22.5° is required to shift from measuring E_x to measuring E_y. Thus, a rotation of the detection crystal is not needed, compared to the case in which a (110) crystal is used. This is clearly preferably in experiments in which the detection crystal is very close to, or in contact with, a sample. When the sample is lying on

the surface of the detection crystal, 2D images are obtained when the crystal/sample is raster scanned, while keeping the probe laser and THz beam fixed. When a more powerful THz beam is used, and employing a modified setup in which the THz-induced polarization changes are translated into probe beam intensity changes, an entire 2D image can be obtained in one shot. This was demonstrated by Doi et al. [62] who measured the spatially resolved THz free-induction decay of a small tyrosine crystal in the near-field.

In the same sense that a focused probe beam can be considered a quasi-aperture, a small sub-wavelength sized THz receiving antenna can also be viewed as a small aperture detector (Fig. 15.8b). This is the approach taken by Bitzer et al. [63, 64] in their measurements of the electric near-field of holes and meta-materials. Their antenna is a small photoconducting antenna consisting of H-shaped electrodes with a 10 μm gap, which allows for the measurements of the in-plane electric-field components of the electric near-field. They obtain a spatial resolution of about 20 μm while holding their antenna some 30 μm from their samples, which is more than sufficient to provide spectacular measurements of the time-dependent electric fields near various metal samples, which will be discussed in more detail in the next section. One advantage of their setup is that the detecting chip together with the probe laser can freely be scanned parallel to the sample surface, allowing them to sample the near field over relatively large areas. By tapering the antenna, the spatial resolution can further be improved. This was shown to be an excellent method to further improve the spatial resolution [65–67]. With an electrode spacing of 1.8 μm at the apex of the electrodes, a spatial resolution of better than 5 μm was demonstrated.

Using yet another approach, calculations suggest that using plasmonic dimer antennas, fabricated from doped semiconductors, it may be possible to confine and enhance the THz electric field inside the gap between the two arms of the antenna. By controlling the carrier density, this enhancement and localization can be controlled with possible applications in spectroscopy and imaging [68].

15.4 Near-Field Imaging

As mentioned in the introduction, near-field imaging can be applied to the study of charge carriers, lattice vibrations of organic and inorganic crystals, and also of the THz electromagnetic near-field itself. We will start this section with the results of imaging the near-field of small metal structures, such as slits and holes. The reason for this is that the information gathered on these structures increases our understanding of other techniques that use small metal structures to obtain a sub-wavelength spatial resolution, such as antennas and holes.

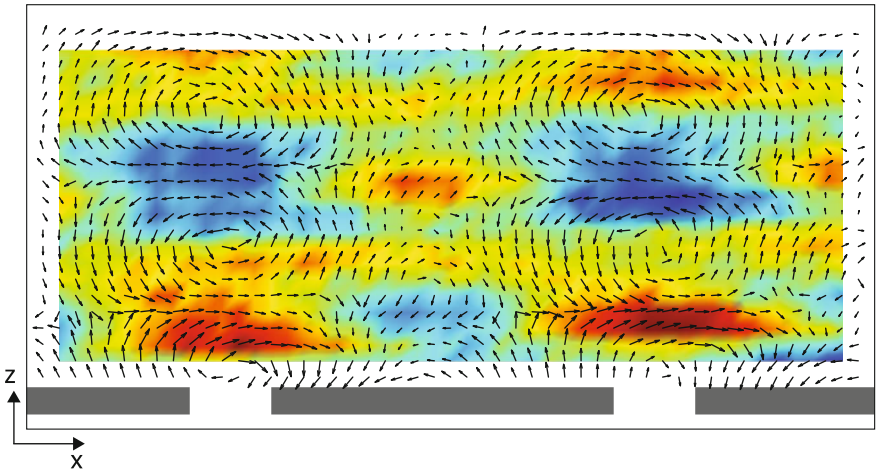

Fig. 15.9 THz electric near-field (vectors) measured behind a metal foil (*dark gray*) in which multiple, 100 μm wide slits were milled with a period of 500 μm. The THz beam is incident from below. The magnetic field component B_y, calculated from the electric field, is shown in color. *Red* and *blue* correspond to opposite magnetic field directions. The size of the entire scan is 1,050 μm in the x-direction and 450 μm in the z-direction. Adapted from [72]

15.4.1 Imaging the THz Electric Near-Field

Using the quasi-aperture techniques described in Sect. 15.3, it is possible to measure the electric near-field with a deep sub-wavelength spatial resolution. In near-field electro-optic detection, in principle, all three orthogonal components of the THz electric near-field can be measured, although symmetry often reduces the required number of components to be measured to two. (In fact, something resembling this can also be done in the visible, see for example Lee et al. [69–71]). This was shown in an experiment by Seo et al. [72] and Ahn et al. [73] in which the THz electric near-field was measured behind a sample consisting of 100 μm wide slits cut in a metal foil with a period of 500 μm. In this experiment, a broadband single cycle THz pulse with a polarization perpendicular to the slits in the x-direction, is incident from below. A 300 μm thick (100) oriented GaP crystal was used to measure the z-component of the electric near-field, which is the component perpendicular to the metal. A (110) oriented GaP crystal was used to measure the x-component polarized parallel to the metal. Due to the symmetry of the sample, no y-component was present. By combining E_x and E_z, the complete time-dependent THz electric field behind the slits could be obtained. From the measurements, a 2D plot of the electric field vector behind the slits can be constructed at any frequency contained in the bandwidth of the single cycle pulse. An example is shown in Fig. 15.9, in which the electric field vector at a frequency of 1 THz is plotted for a fixed phase, representing a single frame from a movie showing the time evolution of the field during one complete cycle at this frequency. The figure shows vortices and saddle points in the field

behind the slits. The distance in the z-direction between the center of two vortices, is 300 μm, corresponding to a frequency of 1 THz. The measurement provides a very nice demonstration of a property of time-dependent electric fields, namely that they must have a nonzero curl according to,

$$\nabla \times \mathbf{E} = -\frac{\partial \mathbf{B}}{\partial t}. \tag{15.6}$$

Using this equation, the electric field measurement shown in Fig. 15.9 can be used to calculate the THz magnetic field component B_y, as shown in the figure in color. With both **E** and **B** known, other properties of the THz light can also be obtained such as the Poynting vector [72]. Again, this shows the advantage of measuring the THz electric field, rather than the intensity. Incidentally, one interesting aspect of slits is that when the width becomes smaller, the transmission can still be considerable leading to an enormously enhanced field inside the slit [74–76].

Of interest for near-field imaging using apertures, is the electric near-field in the immediate neighborhood of an aperture itself. This can be measured with great accuracy by depositing a metal layer, in which the aperture is defined, directly on top of the electro-optic detection crystal. The aperture is then illuminated with a broadband single cycle THz pulses polarized parallel to the crystal in the x-direction. Figure 15.10a–c shows the components of the electric near field $|E_x|$, $|E_y|$, and $|E_z|$, measured immediately underneath a 150 μm diameter aperture in a 200 nm thick gold layer deposited on the GaP electro-optic detection crystal, at a frequency of 0.2 THz [77]. Again, a (100) crystal was used to detect E_z, whereas a (111) crystal was used to measure E_x and E_y. The figures clearly illustrate that the E_x and E_y components are mostly localized inside the aperture, whereas the z-component of the field is mostly confined to the edges of the aperture. This agrees very well with the predictions made by the model from Bouwkamp [37, 38] and by numerical calculations. The measurements also show that this particular measurement technique measures the field very close to aperture, since for increasing distances to the metal plane, the extent of the field should increase rapidly in the x and y directions. However, E_z is not entirely zero inside the aperture and $E_{x,y}$ are not exactly zero outside the aperture, indicating that the field is not measured exactly in the plane of the aperture but, on average, some 10 μm below it.

As in the case of the slits, the components of the measured field can be combined, in this case E_x and E_y, into a single in-plane electric field vector. This is shown in Fig. 15.10d, where the in-plane field vector at the frequency of 0.2 THz is plotted. In Fig. 15.10e, the field calculated using the model from Bouwkamp is shown, where the length of the calculated field vectors near the edge of the aperture is artificially reduced, since the Bouwkamp model predicts unphysical, infinitely strong fields there. The calculation can thus only be used to compare the *direction* of the field, not the strength. Keeping this in mind, it is clear that the measurements and the calculation are in excellent agreement. Although the incident field is polarized in the x-direction, immediately behind the aperture, all three components of the electric field are present. In fact, the measurements constitute a clear illustration of the boundary conditions

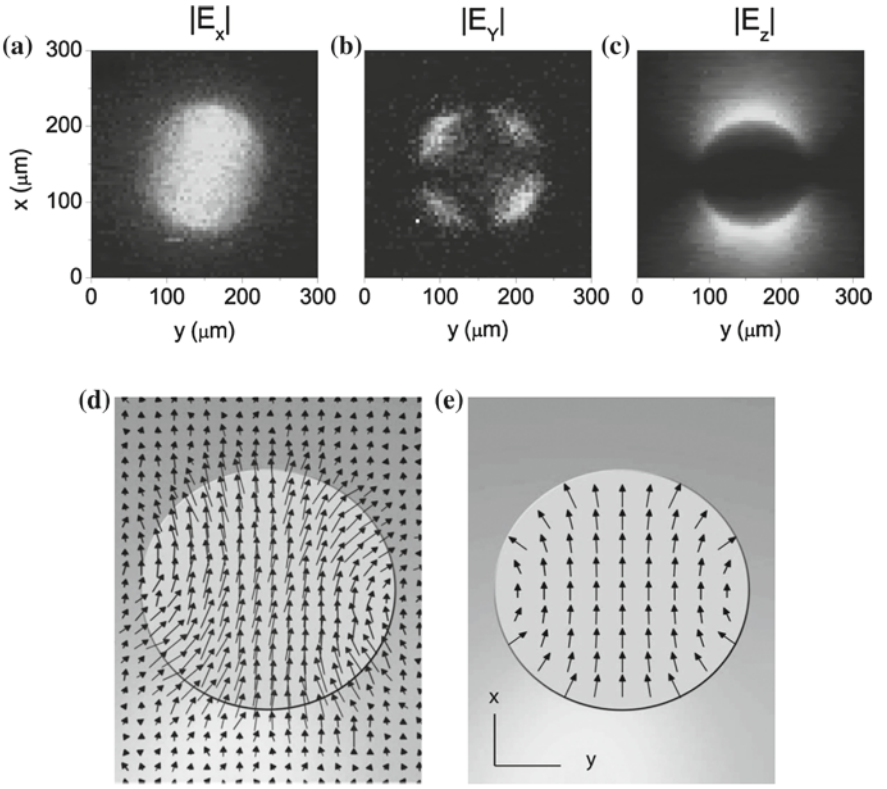

Fig. 15.10 THz electric near-field for a single, isolated, circular aperture ($d = 150\,\mu$m) at 0.2 THz. **a–c** $|E_x|$, $|E_y|$, and $|E_z|$. Scan area $= 315 \times 315\,\mu$m; **d** vector field plot illustrating measured transverse components of THz electric near-field; **e** vector field plot based on the model from Bouwkamp. Adapted from [77]

for the electric field at the interface between a perfect metal and a dielectric. These conditions state that at the metal, the component of the field parallel to the metal should be zero. At the metal, only a component perpendicular to the metal can exist. The shape of the aperture forces the creation of a component perpendicular to the metal surface and the metal e.g., thus explaining the creation of both E_y and E_z. The exact shape of the aperture determines the relative size of the three components. For a square aperture, for example, the E_y component is very small and, in fact, quite difficult to measure [77].

A clear advantage of the ability to measure the electric field, rather than the intensity is that it makes it possible to extract more information from the measurements without the need to make further assumptions about the system. For example, the boundary conditions for the component of the electric field perpendicular to the metal surface, E_z, state that this component is discontinuous with an amount proportional to the surface charge density σ. At the metal surface ($z = 0$), we can write for the

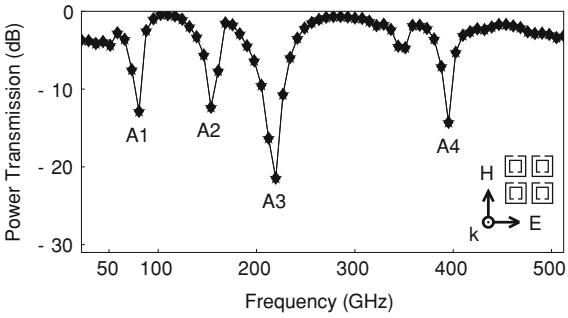

Fig. 15.11 Far-field power transmission spectrum of a split-ring resonator array sample. Four dominant resonances (A1–A4) are observed for an incident field polarization direction as indicated in the *inset*. Adapted from [64]

time- and position-dependent surface-charge density,

$$\sigma(x, y, 0, t) = E_z(x, y, 0, t)/\varepsilon, \tag{15.7}$$

where $\varepsilon = \varepsilon_r \varepsilon_0$ is the permittivity of the dielectric, in this case, the GaP crystal. The plot of the z-component of the electric field, therefore, can also be interpreted as a plot of the surface-charge density. In view of the fact that in reality the field is measured a little distance away from the metal, this is approximately true only, explaining why a small but nonzero E_z is also measured inside the aperture. It must be emphasized that the measurements of the near-field of the hole shown here, actually represent measurements of a metallic aperture *on a dielectric substrate*, not an isolated aperture in free space. Some large and some subtle effects occur as a result of the presence of the substrate, such as an increased transmission at low frequencies, and these also depend on the thickness of the metal [78]. One consequence of the use of a thin (thin compared to the wavelength) metal layer, is that there is no real waveguide cut-off apparent in the near-field measurements. The obvious explanation for this is that for a thin metal, one cannot really speak of a waveguide. As discussed earlier in this chapter, below the "cut-off" frequency of a hole in a thin metal layer, the near-field amplitude decreases linearly with frequency. This means that reasonably large near-fields can be measured at frequencies considerably below the cut-off frequency of a conventional waveguide, illustrating the potential of these apertures for near-field imaging [79, 80], and near-field microspectroscopy of very small samples [81].

Electro-optic near-field imaging has, in addition to holes and slits, been applied to the study of spheres [82], hole arrays [77], photonic-crystal fibers [83] and, using a somewhat different geometry, THz surface waves [84].

Bitzer et al. [64] used photoconducting antennas to measure the near-field of THz meta-materials. Meta-materials are materials with optical properties that do not exist in nature. Typically, their properties are determined by performing far-field measurements, but these only provide indirect clues as to the physical processes going on in the immediate neighborhood of these structures. In Fig. 15.11 the far-field power transmission is shown as a function of frequency for a meta-material sample consisting of split-ring resonators (SRR's), as shown in the inset. The resonators are made of 9 μm thick copper on a 120 μm thick polytetrafluoroethene (PTFE) substrate and

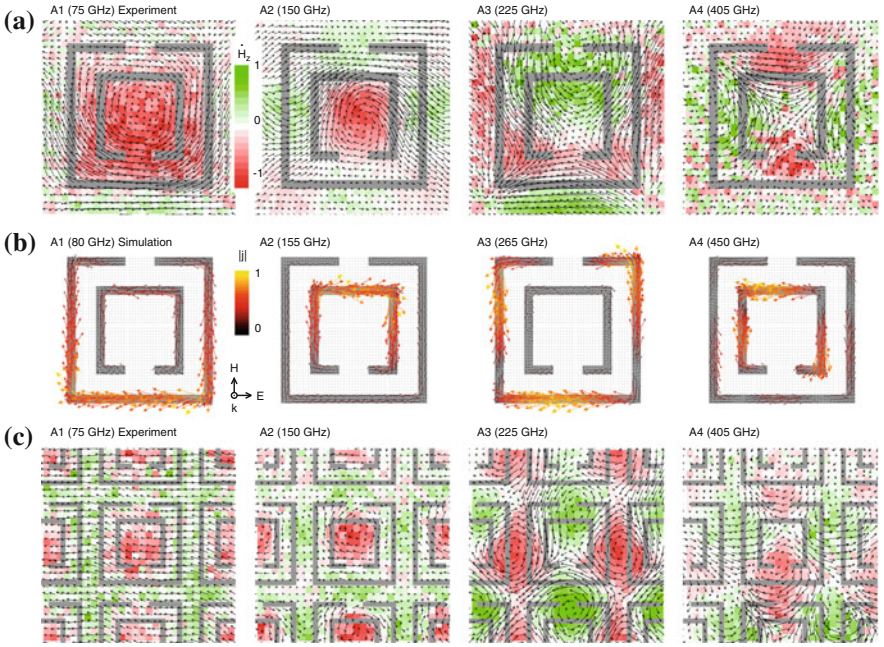

Fig. 15.12 **a** Measured in-plane THz electric near-field (vectors) at a chosen phase at the backside of an isolated split-ring resonator, for the four different resonances A1–A4 shown in Fig. 15.11. The *color code* indicates the time-derivative of the out-of-plane component of the corresponding magnetic field $\partial H_z/\partial t$, derived from the electric field measurements; **b** simulation of the surface current density for a polarization and propagation direction as indicated in the figure; **c** measured in-plane THz electric near-field (vectors) at a chosen phase and $\partial H_z/\partial t$ calculated from the in-plane electric field, at the backside of a split-ring resonator *array*, for the four different resonances A1–A4 shown in Fig. 15.11. Adapted from [64]

their far-field spectrum was measured with a conventional THz time-domain spectroscopy setup. The incident field is polarized in the direction indicated in the figure. Four resonances are clearly observed, corresponding to fundamental excitations of the resonators. Based on these measurements, however, it is not immediately clear what these resonances look like. This can only be observed by performing near-field measurements.

Figure 15.12a shows the 2D spatial distribution of the in-plane, electric near-field vector of a single, isolated, SRR measured with a photoconductive antenna, for four different frequencies corresponding to the four resonances shown in Fig. 15.11 [64]. In the same figure, the magnetic field perpendicular to the plane, calculated from the measured in-plane electric field is also shown. The spatial resolution is on the order of 20 μm. The figure clearly shows distinct electric and magnetic field patterns corresponding to the different SRR modes, where the electric patterns of the modes at 225 and 405 GHz show evidence of an electric quadrupole pattern. Similar measurements on an array of SRR's are plotted in Fig. 15.12c. They show

destructive (A1 mode) and constructive (A3 mode) interference due to the spatially overlapping fields of individual resonators, whereas the other two modes (A2, A4) remain relatively unperturbed. Figure 15.12b shows simulated surface current densities that correspond to the four resonant modes. The calculations of the currents are fully consistent with the measured magnetic field patterns. These and other [85–89] near-field measurements on metamaterials thus provide essential information on the operation of these important structures.

Wächter et al. [65] have used their tapered photoconductive antenna's to obtain a near-field spatial resolution of about 5 μm. Their probe uses a triangular, 1.3 μm thick piece of low-temperature grown GaAs on which the planar tapered wire is fabricated. Near the apex, the gap between the electrodes is 1.8 μm. The resolution was tested by imaging a single element of a frequency-selective surface. The outline and dimensions of this element, an asymmetric double-split metallic ring resonator, are shown in Fig. 15.13a. Interestingly, the element is hidden under a layer of black wax, rendering the element invisible. The sample is illuminated by a photoconductive THz emitter located in the near-field of the detector. In Fig. 15.13b, the THz near-field peak image, created by plotting the measured THz peak amplitude spatial distribution, is plotted. The image clearly reveals the hidden ring resonator and the gaps between the metallic lines. Two line scans, one in the x-direction and one in the y direction across the metallic stripes show the excellent spatial resolution of about 5 μm (x-direction) and 7 μm (y-direction) that were obtained in this experiment. In a different experiment, a near-field line scan was made across a metallic thin film deposited on a transparent substrate. In this case, the THz light, generated at the surface of an InAs crystal, was focused onto the sample using parabolic mirrors. In this very different configuration, a spatial resolution of 4.7 μm was reached, confirming the spatial resolution obtained using near-field illumination. Nagel et al. [90] applied the same near-field technique also to the study of THz emission, locally generated and detected, from an exfoliated graphite flake. In this experiment, however, they used a modified version of their near-field probing tip, by coupling the near field to a tapered single wire, connected to a photoconductive antenna. This makes the system sensitive to the axial near-field, allowing the detection of field components polarized perpendicularly to the graphite surface.

The ultimate spatial resolution in THz imaging so far was obtained by Huber et al. [13]. In a THz ANSOM experiment, they studied the THz near-field response of a single semiconductor nanodevice with a spatial resolution of about 40 nm. To obtain this resolution a relatively powerful THz source was used, namely a methanol gas laser with an output power of 5 mW, pumped by a CO_2 laser. In their experiment, a platinum covered atomic force microscope (AFM) tip is illuminated with the THz light at a frequency of 2.54 THz. The THz light backscattered from the tip is measured using a hot-electron bolometer in conjunction with a Michelson interferometer to amplify the signal. The tip is vibrated at a frequency of 35 kHz, and the measured signal is demodulated at the second or third harmonic of that frequency to obtain background-free detection. Figure 15.14a–c shows an AFM image, a THz ANSOM image, and an IR ANSOM image obtained at a wavelength of 11 μm, respectively, of a polished cut through a multiple transistor device. The charge carrier concentrations

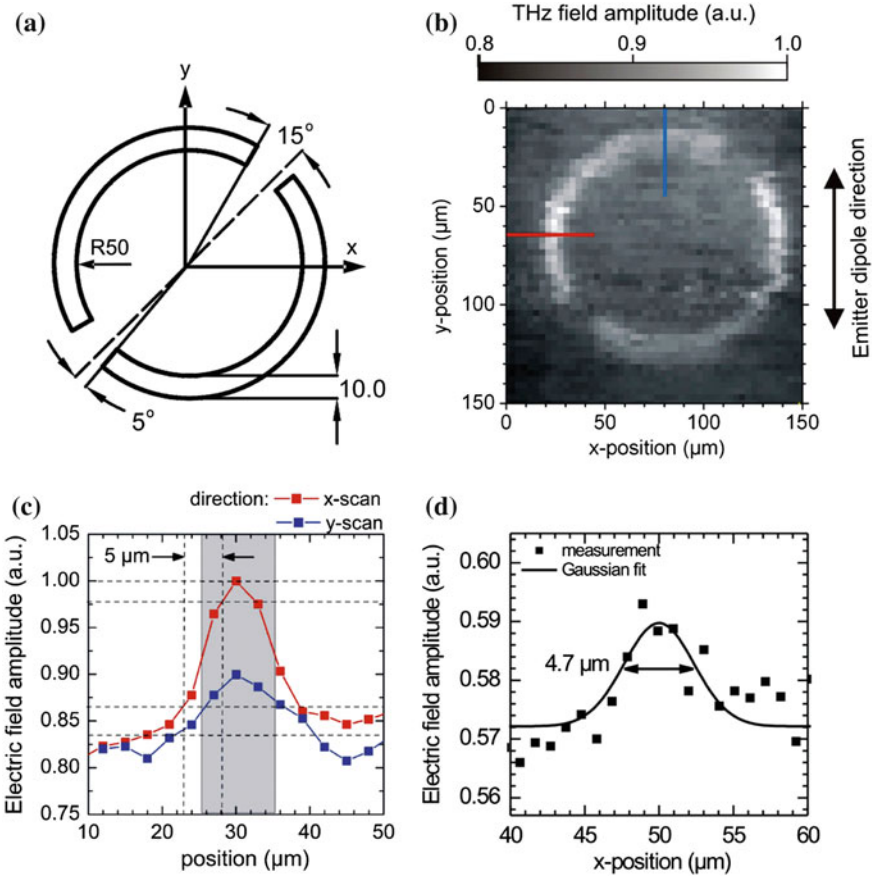

Fig. 15.13 **a** Outline and dimensions of a single element of an asymmetric double-split metallic ring resonator; **b** THz near-field amplitude image of the sample, obtained using a tapered photoconductive antenna. Pixels are $3 \times 3\,\mu m^2$ in size; **c** field amplitude as a function of position along *two lines* across the $10\,\mu m$ wide metallic structure, one in the x-direction the other in the y-direction. Lines are indicated in **b**; **d** measured THz electric field amplitude as a function of position along a line perpendicular to a metallic edge illuminated by THz light incident from the far-field. Adapted from [65]

present in this device at various depths, are also indicated in (b) and (c). This clearly shows that only in the THz image the different carrier concentrations are recognizable. The reason for this is demonstrated in the Fig. 15.14e, which is a calculation of the scattered signal, detected at the second harmonic of the modulation frequency, as a function of THz frequency for carrier concentrations ranging from 10^{16} to 10^{19} cm^{-3}. The graph shows that in the range of carrier concentrations typically present in these devices, THz radiation provides the best possible image contrast because the THz frequency is close to the typical plasma frequencies that correspond to these

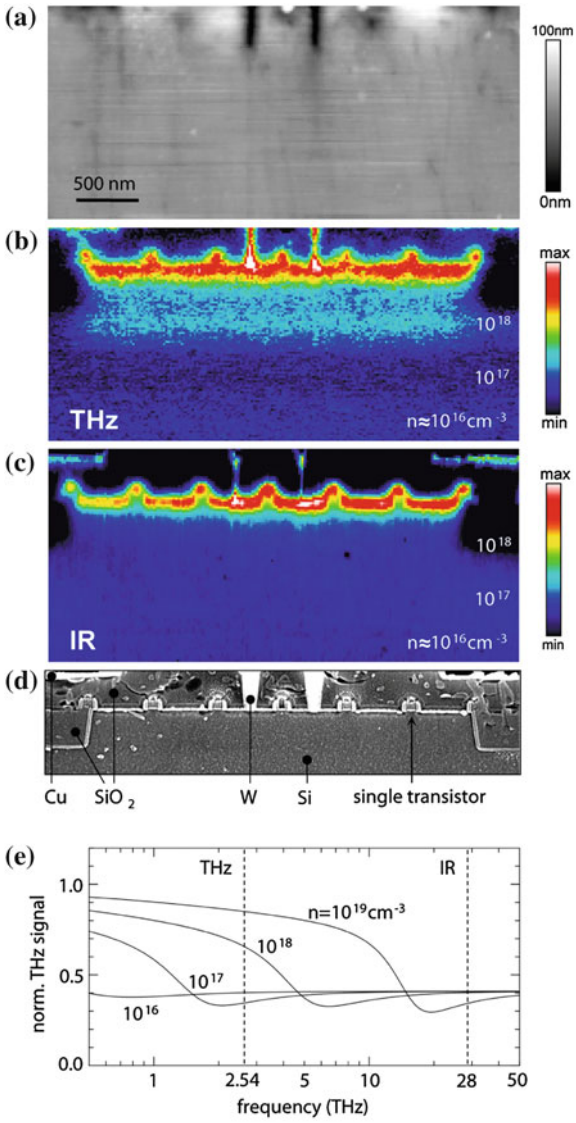

Fig. 15.14 **a** AFM image of a polished cut through a multiple transistor device; **b** THz image simultaneously obtained with the AFM image at the second harmonic of the modulation frequency; **c** infrared image ($\lambda = 11\,\mu$m) obtained by measuring the scattered infrared light at the second harmonic of the modulation frequency. The mobile carrier concentrations in **b** and **c** are indicated in the figure, on the *right-hand side*; **d** SEM image of part of the device marked by the *rectangle*; **e** THz signal amplitude detected at the second harmonic of the modulation frequency, as a function of light frequency, for several carrier concentrations. Adapted from [13]

carrier concentrations. In other words, the THz signal varies more strongly with these typical carrier concentrations than the signal at infrared wavelengths, as shown in the figure [91]. In Fig. 15.14d, a SEM image of a small part of the device, outlined by the rectangle in (a) and (b), is shown, providing information on the structure of the device. The results are particularly spectacular when the obtained spatial resolution is expressed as a fraction of the wavelength. A frequency of 2.54 THz corresponds to a wavelength of about $\lambda = 118\,\mu$m. This means that the 40 nm spatial resolution

corresponds to about $\lambda/3{,}000$, something that is very difficult to achieve in the visible region of the electromagnetic spectrum.

15.5 Conclusions and Outlook

It is clear that THz near-field imaging and spectroscopy constitute an active and promising branch on the "THz tree". It is only natural to speculate on the directions in which this "branch" will grow. The results by Huber et al. [13] show that the measurement of carriers on the nanoscale forms a very interesting application of THz nanoscopy. In addition, it is clear that THz-TDS is a very powerful technique to probe the time-dependent electric field of light itself on deep subwavelength scales. The information gathered in the THz frequency range will have important implications in the visible region of the electromagnetic spectrum as well since Maxwell's equations are scale-invariant and only the material properties are somewhat different. In the THz frequency range, however, measurements can be done that are difficult or impossible to do in the visible. For example, it is currently not possible to have a sub-wavelength spatial resolution *and*, simultaneously, a sub-cycle temporal resolution in the visible. Add to that the enormously broad spectrum of many pulsed THz sources and it becomes clear that the capabilities that THz near-field microscopy offers are quite remarkable compared to what is currently possible with visible light. Not all is well, however, since it will be hard to extend the nanoscopy measurements on carriers to, for example, lattice modes of organic molecular crystals, which are fairly weakly absorbing compared to the strong absorbing lattice modes of simpler crystals like GaAs. Still, with current techniques to generate and detect THz light at higher and higher frequencies (see for example Sell et al. [92]) it is probably only a matter of time before these techniques can be applied also to, for example, the molecular fingerprint region of the electromagnetic spectrum. The near-field techniques developed for the THz frequency region are thus seen to have an impact on other regions of the electromagnetic spectrum. Their importance can thus not easily be overestimated. There is a bright future for THz near-field imaging.

References

1. M. Specht, J.D. Pedarnig, W.M. Heckl, T.W. Hänsch, Phys. Rev. Lett. **68**, 476 (1992)
2. F. Zenhausern, Y. Martin, H.K. Wickramasinghe, Science **269**, 1083 (1995)
3. B. Knoll, F. Keilmann, Nature **399**, 134 (1999)
4. B. Knoll, F. Keilmann, Opt. Commun. **182**, 321 (2000)
5. R. Hillenbrand, T. Taubner, F. Keilmann, Nature **418**, 159 (2002)
6. N.C.J. van der Valk, P.C.M. Planken, Appl. Phys. Lett. **81**, 1558 (2002)
7. P.C.M. Planken, C.E.W.M. van Rijmenam, R.N. Schouten, Semicond. Sci. Technol. **20**, s121 (2005)
8. W.A. Kütt, W. Albrecht, H. Kurz, IEEE J. Quantum Electron. **28**, 2434 (1992)

9. R. Adam, L. Chusseau, T. Grosjean, A. Penarier, J.-P. Guillet, D. Charraut, J. Appl. Phys. **106**, 073107 (2009)
10. H.-T. Chen, R. Kersting, G.C. Cho, Appl. Phys. Lett. **83**, 3009 (2003)
11. G.C. Cho, H.-T. Chen, S. Kraatz, N. Karpowicz, R. Kersting, Semicond. Sci. Technol. **20**, S286 (2005)
12. F. Buersgens, R. Kersting, H.-T. Chen, Appl. Phys. Lett. **88**, 112115 (2006)
13. A.J. Huber, F. Keilmann, J. Wittborn, J. Aizpura, R. Hillenbrand, Nano Lett. **8**, 3766 (2008)
14. A.J.L. Adam, N.C.J. van der Valk, P.C.M. Planken, J. Opt. Soc. Am. B **24**, 1080 (2007)
15. K. Wang, D.M. Mittleman, N.C.J. van der Valk, P.C.M. Planken, Appl. Phys. Lett. **85**, 2715 (2004)
16. H.-T. Chen, S. Kraatz, G.C. Cho, R. Kersting, Phys. Rev. Lett. **93**, 267401 (2004)
17. R. Kersting, H.-T. Chen, N. Karpowicz, G.C. Cho, J. Appl. Opt. Pure Appl. Opt. **7**, s184 (2005)
18. Y. Li, S. Popov, A.T. Friberg, S. Sergeyev, J. Eur. Opt. Soc. Rap. Public **4**, 09007 (2009)
19. M. Walther, G.S. Chambers, Z. Liu, M.R. Freeman, F.A. Hegmann, J. Opt. Soc. Am. B **22**, 2357 (2005)
20. C.A. Balanis, *Antenna Theory, Analysis and Design*, 2nd edn. (Wiley, New York, 1997)
21. J. van Bladel, Proc. IEEE **71**, 901 (1983)
22. H. Cory, A.C. Boccara, J.C. Rivoal, A. Lahrech, Microwave Opt. Technol. Lett. **18**, 120 (1998)
23. K. Wang, D.M. Mittleman, Nature **432**, 376 (2004)
24. K. Wang, A. Barkan, D.M. Mittleman, Appl. Phys. Lett. **84**, 305 (2004)
25. K. Wang, D.M. Mittleman, Phys. Rev. Lett. **96**, 157401 (2006)
26. V. Astley, R. Mendis, D.M. Mittleman, Appl. Phys. Lett. **95**, 031104 (2009)
27. J.A. Deibel, N. Berndsen, K. Wang, D.M. Mittleman, N.C.J. van der Valk, P.C.M. Planken, Opt. Express **14**, 8772 (2006)
28. A. Agrawal, A. Nahata, Opt. Express **15**, 9022 (2007)
29. J.A. Deibel, K. Wang, M.D. Escarra, D.M. Mittleman, Opt. Express **14**, 279 (2006)
30. M. Awad, M. Nagel, H. Kurz, Appl. Phys. Lett. **94**, 051107 (2009)
31. H. Zhan, V. Astley, M. Hvasta, J.A. Deibel, D.M. Mittleman, Appl. Phys. Lett. **91**, 162110 (2007)
32. S.A. Maier, S.R. Andrews, L. Martín-Moreno, F.J. García-Vidal, Phys. Rev. lett. **97**, 176805 (2006)
33. H. Liang, S. Ruan, M. Zhang, H. Su, Opt. Commun. **283**, 262 (2010)
34. F. Keilmann, Infrared Phys. Technol. **36**, 217 (1995)
35. S. Hunsche, M. Koch, I. Brener, M.C. Nuss, Opt. Commun. **150**, 22 (1998)
36. H.A. Bethe, Phys. Rev. **66**, 163 (1944)
37. C.J. Bouwkamp, Philips Res. Rep. **5**, 321 (1950)
38. C.J. Bouwkamp, Philips Res. Rep. **5**, 401 (1950)
39. O. Mitrofanov, I. Brener, M.C. Wanke, R.R. Ruel, J.D. Wynn, A.J. Bruce, J. Federici, Appl. Phys. Lett. **77**, 591 (2000)
40. O. Mitrofanov, I. Brener, R. Harel, J.D. Wynn, L.N. Pfeiffer, K.W. West, J. Federici, Appl. Phys. Lett. **77**, 3496 (2000)
41. O. Mitrofanov, M. Lee, J.W.P. Hsu, L.N. Pfeiffer, K.W. West, J.D. Wynn, J.F. Federici, Appl. Phys. Lett. **79**, 907 (2001)
42. O. Mitrofanov, R. Harel, M. Lee, L.N. Pfeiffer, K.W. West, J.D. Wynn, J. Federici, Appl. Phys. Lett. **78**, 252 (2001)
43. O. Mitrofanov, M. Lee, J.W.P. Hsu, R. Harel, J.F. Federici, J.D. Wynn, L.N. Pfeiffer, K.W. West, IEEE J. Sel. Top. Quantum Electron. **7**, 600 (2001)
44. O. Mitrofanov, L.N. Pfeiffer, K.W. West, Appl. Phys. Lett. **81**, 1579 (2002)
45. O. Mitrofanov et al., *Ultrafast Phenomena XIII, Proceedings, Springer series in Chemical Physics*, 2003, p. 286
46. A.J.L. Adam, J.M. Brok, M.A. Seo, K.J. Ahn, D.S. Kim, J.H. Kang, Q.H. Park, M. Nagel, P.C.M. Planken, Opt. Express **16**, 7407 (2008)
47. A. Agrawal, H. Cao, A. Nahata, Opt. Express **13**, 3535 (2005)
48. H. Cao, A. Agrawal, A. Nahata, Opt. Express **13**, 763 (2005)

49. K. Ishihara, G. Hatakoshi, T. Ikari, H. Minamide, H. Ito, K. Ohashi, Jpn. J. Appl. Phys. **44**, L1005 (2005)
50. K. Ishihara, T. Ikari, H. Minamide, J. Shikata, K. Ohashi, H. Yokoyama, H. Ito, Jpn. J. Appl. Phys. **44**, L929 (2005)
51. K. Ishihara, K. Ohashi, T. Ikari, H. Minamide, H. Yokoyama, J. Shikata, H. Ito, Appl. Phys. Lett. **89**, 201120 (2006)
52. Y. Kawano, K. Ishibashi, Nat. Photonics **2**, 618 (2008)
53. J. Zhang, D. Grischkowsky, Appl. Phys. Lett. **86**, 061109 (2005)
54. M.M. Awad, R.A. Cheville, Appl. Phys. Lett. **86**, 221107 (2005)
55. H. Zhan, R. Mendis, D.M. Mittleman, Opt. Express **18**, 9643 (2010)
56. Q. Chen, Z. Jiang, G.X. Xu, X.-C. Zhang, Opt. Lett. **25**, 1122 (2000)
57. Q. Chen, X.-C. Zhang, IEEE J. Sel. Top. Quantum Electron. **7**, 608 (2001)
58. O. Mitrofanov, Appl. Phys. Lett. **88**, 091118 (2006)
59. T. Pfeifer, H.-M. Heiliger, T. Löffler, C. Ohlhoff, C. Meyer, G. Lüpke, H.G. Roskos, H. Kurz, IEEE J. Sel. Top. Quantum Electron. **2**, 586 (1996)
60. K. Yang, L.P.B. Katehi, J.F. Whitaker, Appl. Phys. Lett. **77**, 486 (2000)
61. N.C.J. van der Valk, W.A.M. van der Marel, P.C.M. Planken, Opt. Lett. **30**, 2802 (2005)
62. A. Doi, F. Blanchard, H. Hirori, K. Tanaka, Opt. Express **18**, 18419 (2010)
63. A. Bitzer, M. Walther, Appl. Phys. Lett. **92**, 231101 (2008)
64. A. Bitzer, H. Merbold, A. Thoman, T. Feurer, H. Helm, M. Walther, Opt. Express **17**, 3826 (2009)
65. M. Wächter, M. Nagel, H. Kurz, Appl. Phys. Lett. **95**, 041112 (2009)
66. M. Wächter, C. Matheisen, M. Waldow, T. Wahlbrink, J. Bolten, M. Nagel, H. Kurz, Appl. Phys. Lett. **97**, 161107 (2010)
67. *35th international conference on infrared, millimeter and terahertz waves*, Rome, 2010
68. V. Giannini, A. Berrier, S. Maier, J.A. Sánchez-Gil, J. Gómez Rivas, Opt. Express **18**, 2797 (2010)
69. K.G. Lee, H.W. Kihm, J.E. Kihm, W.J. Choi, H. Kim, C. Ropers, D.J. Park, Y.C. Yoon, S.B. Choi, D.H. Woo, J. Kim, B. Lee, Q.H. Park, C. Lienau, D.S. Kim, Nat. Photonics **1**, 53 (2007)
70. J.S. Ahn, H.W. Kihm, J.E. Kihm, D.S. Kim, K.G. Lee, Opt. Express **17**, 2280 (2009)
71. K.G. Lee, H.W. Kihm, K.J. Ahn, J.S. Ahn, Y.D. Suh, C. Lienau, D.S. Kim, Opt. Express **15**, 14993 (2007)
72. M.A. Seo, A.J.L. Adam, J.H. Kang, J.W. Lee, S.C. Jeoung, Q.H. Park, P.C.M. Planken, D.S. Kim, Opt. Express **15**, 11781 (2007)
73. K.J. Ahn, K.G. Lee, H.W. Kihm, M.A. Seo, A.J.L. Adam, P.C.M. Planken, D.S. Kim, New J. Phys. **10**, 105003 (2008)
74. M.A. Seo, H.R. Park, S.M. Koo, D.J. Park, J.H. Kang, O.K. Suwal, S.S. Choi, P.C.M. Planken, G.S. Park, N.K. Park, Q.H. Park, D.S. Kim, Nat. Photonics **3**, 152 (2009)
75. M.A. Seo, A.J.L. Adam, J.H. Kang, J.W. Lee, K.J. Ahn, Q.H. Park, P.C.M. Planken, D.S. Kim, Opt. Express **16**, 20484 (2008)
76. M.A. Seo, H.R. Park, D.J. Park, D.S. Kim, A.J.L. Adam, P.C.M. Planken, J. Korean Phys. Soc. **55**, 267 (2009)
77. J.R. Knab, A.J.L. Adam, M. Nagel, E. Shaner, M.A. Seo, D.S. Kim, P.C.M. Planken, Opt. Express **17**, 15072 (2009)
78. L. Guestin, A.J.L. Adam, J.R. Knab, M. Nagel, P.C.M. Planken, Opt. Express **17**, 17412 (2009)
79. O. Mitrofanov, T. Tan, P.R. Mark, B. Bowden, J.A. Harrington, Appl. Phys. Lett. **94**, 171104 (2009)
80. O. Mitrofanov, J.A. Harrington, Opt. Express **18**, 1898 (2010)
81. J.R. Knab, A.J.L. Adam, R. Chakkittakandy, P.C.M. Planken, Appl. Phys. Lett. **97**, 031115 (2010)
82. A.J.L. Adam, J.M. Brok, P.C.M. Planken, M.A. Seo, D.S. Kim, C. R. Phys. **9**, 161 (2008)
83. K. Nielsen, H.K. Rasmussen, A.J.L. Adam, P.C.M. Planken, O. Bang, P.U. Jepsen, Opt. Express **17**, 8592 (2009)
84. W. Zhu, A. Nahata, Opt. Express **15**, 5616 (2007)

85. A. Bitzer, J. Wallauer, H. Helm, H. Merbold, T. Feurer, M. Walther, Opt. Express **17**, 22108 (2009)
86. A. Bitzer, A. Ortner, M. Walther, Appl. Opt. **49**, E1 (2010)
87. A. Bitzer, A. Ortner, H. Merbold, T. Feurer, M. Walther, Opt. Express **19**, 2537 (2011)
88. M. Walther, B.M. Fischer, A. Ortner, A. Bitzer, A. Thoman, H. Helm, Anal. Bioanal. Chem. **397**, 1009 (2010)
89. V.A. Fedotov, N. Papasimakis, E. Plum, A. Bitzer, M. Walther, P. Kuo, D.P. Tsai, N.I. Zheludev, Phys. Rev. Lett. **104**, 223901 (2010)
90. M. Nagel, A. Michalski, T. Botzem, H. Kurz, Opt. Express **19**, 4667 (2011)
91. F. Keilmann, A.J. Huber, R. Hillenbrand, J. Infrared Milli, Terahz. Waves **30**, 1255 (2009)
92. A. Sell, A. Leitenstorfer, R. Huber, Opt. Lett. **33**, 2767 (2008)